Subvisual–Thin Cirrus Lidar Dataset for Satellite Verification and Climatological Research

KENNETH SASSEN AND BYUNG SUNG CHO

Department of Meteorology, University of Utah, Salt Lake City, Utah

(Manuscript received 28 August 1991, in final form 7 February 1992)

ABSTRACT

A polarization (0.694-μm wavelength) lidar dataset for subvisual and thin (bluish-colored) cirrus clouds is drawn from Project FIRE (First ISCCP Regional Experiment) extended time observations. The clouds are characterized by their day–night visual appearance; base, top, and optical midcloud heights and temperatures; measured physical (ΔZ) and estimated optical (τ_c) cloud thicknesses; integrated linear depolarization ratios; and derived $k/2\eta$ ratios. A subset of the data supporting 30 NOAA polar-orbiting satellite overpasses is given in tabular form to provide investigators with the means to test cloud retrieval algorithms and establish the limits of cirrus detectability from satellite measurements under various conditions. Climatologically, subvisual–thin cirrus appear to be higher, colder, and more strongly depolarizing than previously reported midlatitude cirrus, although similar $k/2\eta$ that decrease with height and temperature are found. A class of radiatively distinct subvisual cirrus with $k/2\eta \leqslant 0.005$ sr^{-1} and possible day–night differences in $k/2\eta$ are indicated. Optical midcloud heights tend to occur somewhat below the actual cloud center in this sample. On average, subvisual to barely visible cirrus display $\tau_c \leqslant 0.03$, $0.03 \leqslant \tau_c \leqslant 0.3$ are indicated for thin cirrus, and an upper limit of $\tau_c \approx 3.0$ is suggested for lidar attenuation-limited opaque cirrostratus (i.e., altostratus).

I. Introduction

There is little doubt that cirrus clouds play an important role in modulating the radiation balance of the earth–atmosphere system, and thus are a significant factor in attempts to understand climate and the prospects for climatic change (for a recent review see Liou 1986). Nonetheless, cirrus remain a missing link in our comprehension of the basic factors controlling atmospheric circulations and climate because, until recently, they have largely escaped critical scientific examination. This situation is rapidly changing, however. In recognition of the importance of characterizing the average and seasonal state of the cloudy atmosphere, including the high-cloud component, the ongoing International Satellite Cloud Climatology Program (ISCCP) is being directed toward accumulating an extensive, long-term satellite observational database (Schiffer and Rossow 1983). Since it was generally accepted, however, that considerable uncertainties were involved in detecting and characterizing clouds, and cirrus in particular, spin-off research programs, such as the First ISCCP Regional Experiment (FIRE) in the United States, the European International Cirrus Experiment (ICE), and the Experimental Cloud Lidar Pilot Study (ECLIPS) with worldwide participation, are researching the means to address this problem. Polarization lidar, with its nearly ideal sensitivity to cirrus cloud particles, is a key element in these endeavors.

In this paper we address a topic of fundamental concern to both improving our knowledge of cirrus-cloud properties and the approaches used for studying them from satellites and ground-based lidars. Namely, we present a polarization lidar dataset derived from Project FIRE extended time observations (ETO) of subvisual and optically thin cirrus clouds, which obviously represent a major challenge to satellite cloud retrieval methods. By compiling appropriate data in support of a number of local NOAA polar-orbiting satellite overpasses, we hope to provide researchers involved in testing and developing improved cloud-detection algorithms with the means to evaluate their approaches. At the same time, the climatological properties derived from these and additional cirrus add to our basic knowledge of these common but poorly understood varieties of cirrus clouds. Particular attention is given to the examination of basic lidar scattering parameters to improve the utility of lidar for cirrus cloud–climate research.

2. The nature of the dataset

Our ongoing FIRE ETO cirrus research program, based at the University of Utah Facility for Atmospheric Remote Sensing (FARS) in Salt Lake City (40°46′00″N, 111°49′38″W), was initiated in De-

Corresponding author address: Dr. Kenneth Sassen, University of Utah, Department of Meteorology, 819 William C. Browning Building, Salt Lake City, UT 84112.

cember 1986. Although the evolving cloud remote-sensing capabilities have steadily improved since that time, and currently include a variety of visible and infrared radiometers, K_a-band microwave radar, and video cloud imaging systems, the key apparatus relied on in this study are a zenith-pointing, dual-polarization ruby (0.694-μm wavelength) lidar system (see Sassen et al. 1989a for unit specifications), and color and black-and-white fish-eye cameras. All-sky cloud images (during daylight) and field notes are recorded at regular intervals and at the times of local polar-orbiting and Geostationary Operational Environmental Satellite (GOES) imagery to characterize global and zenith cloud conditions. On the basis of this information, as described following, a characterization of the visual cirrus cloud properties is determined. Note that FARS is located at an elevation of 1.52 km above mean sea level (MSL) in the western foothills of the Wasatch Mountains, 12 km west of the local National Weather Service radiosonde station.

The cirrus clouds considered here are divided into five categories. For daylight studies, the cirrus (in the zenith direction where the lidar is pointed) are categorized as subvisual, threshold visible, and thin (i.e., bluish colored). The distinction between subvisual and threshold (i.e., barely visible or grayish appearing) cirrus often depends on the solar elevation angle, since strong forward scattering in the vicinity of the solar disk increases the visibility of the clouds overhead near local noon. Other factors include lower-atmospheric turbidity (e.g., boundary-layer haze) and spatial cloud density variations, which enable visual cloud detection through contrast considerations (particularly when viewed through a polarizing filter). For nocturnal ETO studies (included here to provide data free from solar contamination of near-infrared channel radiances), two cloud categories are employed. These represent cases in which some stars are dimly visible through the thin cirrus near the zenith, or when improved visibility does not noticeably restrict the visualization of stars. (These studies were normally done only if some cirrus were observed visually or were expected on the basis of satellite imagery.) Obviously, these categories are subjective in nature, but on average a useful image of the corresponding cloud optical properties should emerge by treating a large sample.

The data quantities derived from the lidar measurements include the cirrus cloud base, top, and effective midcloud altitudes Z_{cb}, Z_{ct}, and Z_e; the scattering ratio R; the physical and optical cloud thicknesses ΔZ and τ_c; and the linear depolarization ratio Δ integrated vertically through the cloud, all determined from a single dual-channel lidar return profile representing the average of a number a consecutive lidar shots. (Typically, approximately 20 shots collected at the maximum pulse repetition frequency (PRF) over a 10-min period bracketing the overpass time are averaged, although longer periods have been used for relatively weak signals or reduced PRF observations.) The cirrus effective (i.e., optical) midcloud height, defined as the height at which equal cloud optical thicknesses are found below and aloft (see Grund and Eloranta 1990), is converted to temperature T_e along with the cloud-base and cloud-top temperatures T_{cb} and T_{ct} on the basis of local sounding data. Note that the cloud-base and cloud-top heights are defined with reference to a scattering ratio $R \geqslant 1.5$, where

$$R(z) = \frac{\beta'_m(z)_{\|} + \beta'_c(z)_{\|}}{\beta'_m(z)_{\|}}, \tag{1}$$

and the volume backscattering coefficients $\beta'(z)$ in the parallel ($\|$) polarization plane are subscripted according to the molecular m and cloud c components. Similarly, Δ is computed for $R \geqslant 3$ (to lessen the impact of molecular scattering on cloud depolarization) from

$$\Delta(z) = \frac{\sum \beta'_t(z)_{\perp}}{\sum \beta'_t(z)_{\|}}, \tag{2}$$

where $\perp$ identifies the perpendicular polarized channel and the total backscatter coefficient $\beta'_t(z) = \beta'_m(z) + \beta'_c(z)$.

The numerical procedure involves the calibration of the lidar equation in each case based on the pure molecular scattering assumption below the cirrus cloud base (see the Appendix). An atmospheric profile of $\beta'_m(z)$ is generated from the air density obtained from local sounding data, and the minimum in the vertically and temporally averaged lidar return (found by searching the region below an input approximate Z_{cb}) is matched to the β'_m at that altitude. Once the cloud base is identified, $\beta'_c(z)$ is computed from $\beta'_t(z) - \beta'_m(z)$ after attempting to correct for the effects of attenuation from air and cloud particles. The first correction is straightforward, but the second can be treated only in an approximate manner.

Cirrus cloud extinction coefficients currently must be assumed to be related linearly to β'_c through the use of an invariant-with-height backscatter-to-extinction ratio k; another complication is caused by laser light that is multiply scattered between cloud particles before being returned to the receiver. A multiple-scattering correction factor η can be employed in effect to decrease the cloud extinction rate, thereby accounting for the strong diffraction-dominated forward scattering that would remain indefinitely within the laser pulse. Another approach (Platt 1979) treats η as part of the combined term $k/2\eta$, and in essence is meant to include all detected multiple backscattering regardless of the process involved. We use analysis methods based on both approaches in this study.

Method A specifies a range of k derived from ray-tracing simulations of simple hexagonal ice crystal shapes (see Sassen et al. 1989b), including thin-plate ($k = 0.026$ sr^{-1}), thick-plate (0.086 sr^{-1}), and column (0.038 sr^{-1}) models. For comparison, recent high

spectral resolution lidar studies of a cirrostratus cloud (Grund and Eloranta 1990) measured backscatter phase functions (equivalent to k in the absence of absorption) ranging from approximately 0.02 to 0.045 sr^{-1}. A value of $\eta = 0.75$ is specified when these k are used, which takes into consideration (according to generic model predictions based on our lidar receiver geometry and diffraction theory for typically sized cirrus ice crystals) forward scattering that would be effective in generating backscattering (see Appendix). Method B is also based on the subcloud pure molecular scattering assumption, but uses an iterative approach to solving the lidar equation that varies the value of $k/2\eta$ to maximize the agreement of the derived and sounding-based β'_m above cirrus cloud top. This method attempts to derive an average $R = 1.0$ in the data points extending 500 m above the cirrus cloud top as a function of $k/2\eta$. However, molecular scattering in the upper troposphere at the ruby laser wavelength is quite weak even without the attenuation produced by cirrus, so in practice this method cannot be applied under all conditions. [Moreover, many of our data records do not extend sufficiently far enough above cirrus cloud top, while the effects of noise in extremely weak signals can lead to $0.001\ sr^{-1} \leqslant k/2\eta \geqslant 0.1\ sr^{-1}$ that are rejected in our analysis, based on the bounds in values reported by Sassen (1978) and Platt et al. (1987).] In either case, the final goal is to derive the cirrus cloud optical thickness

$$\tau_c = \frac{1}{k}\int_{z_{cb}}^{z_{ct}} \beta'_c(z)dz. \tag{3}$$

The values of τ_c given here for subvisual and thin cirrus clouds represent the average of all four numerical results when method B proved reliable (in 70% of the cases with recorded signals extending 0.5 km above cirrus cloud top), and otherwise the average of the three method A values are used. Note that to compute τ_c using method B a $k = 0.05\ sr^{-1}$ (the numerical average of the three theoretical values given earlier) is assumed.

Finally, we introduce the parameter ξ to characterize the relationship between the effective midcloud height and the cloud-base and cloud-top altitudes. This parameter is defined by

$$\xi = \frac{Z_e - Z_{cb}}{\Delta Z} \tag{4}$$

and is used to describe where the relative position of Z_e is found in relation to a normalized cloud-thickness profile (i.e., $\xi \approx 0$ and 1.0 represent optical midcloud positions near cloud base and cloud top, respectively).

3. The FARS satellite verification dataset

Table 1 summarizes our findings from 30 FARS-supported satellite overpasses in terms of the variables previously defined. Note that this sample is equally divided among observations collected during the primary Project FIRE periods (days 5–10 and 20–25 of each month, marked by **), which involve extensive satellite data archival at the FIRE project office,[1] and at other times. Compiled in Table 1 are the date and time of the *NOAA-9, NOAA-10,* or *NOAA-11* satellite local overpass, the cirrus-cloud-type category (see table footnote), the indicated lidar data variables, and some comments on atmospheric conditions.

The dataset in Table 1 represents a diverse range of conditions, including a wide selection of satellite viewing angles and local lighting conditions (i.e., morning—N10, afternoon—N9 and N11, and evening and night—N10 and N11). Indicated in the comments column are factors affecting cirrus cloud visibility (from the ground or satellites), such as local ground snowcover and haze, and also some cirrus cloud properties. These include cirrus containing numerous contrails and displaying optical phenomena. It is significant that corona-producing clouds are present in this sample, since recent research (Sassen 1991a) indicates mean particle sizes of approximately 20 μm for such clouds. Only single-layered clouds are treated.

In selecting this sample we have attempted to concentrate on cirrus clouds whose properties remained reasonably uniform over the approximate 10-min period bracketing the satellite overpass time. (Under typical conditions, this sample length corresponds to a 10- to 20-km-long and approximately 10-m-wide lidar footprint.) In view of possible inaccuracies in satellite navigation and the predicted ephemeris, it is also advisable to treat cirrus that are temporally homogeneous over somewhat longer time scales. Although some cirrostratus would satisfy this criterion over 30-min periods or longer, cirrus often display mesoscale structural variations that decorrelate cloud properties over similar time scales. Given for illustration in Figs. 1 and 2 are height–time displays of lidar backscattering profiles representing both relatively consistent and variable cirrus layers drawn from the satellite verification dataset.

4. Mean cirrus cloud scattering properties

In this section we employ an expanded subvisual–thin cirrus cloud dataset to examine various cirrus properties and the distinctions between the cloud categories. [About one-half of the 92 data samples have been derived from a recent comprehensive three-month FARS program in support of DMSP (Defense Meteorological Satellite Program), FIRE, and ECLIPS satellite observations over March–May 1991.] Specifically, we consider the dependence of τ_c on ΔZ, Δ on T_e, the relative relation between ΔZ and Z_e using the param-

[1] For information regarding FIRE ETO satellite data access, contact L. M. Olsen, Code 634, NASA Goddard Space Flight Center, Greenbelt, MD 20771.

TABLE 1. Historical set of *NOAA-9*, *NOAA-10*, and *NOAA-11* overpasses supported by FARS lidar and sounding data for subvisual–thin cirrus clouds.

Date	Time (UTC)	Satellite	Category*	Z_{cb} (km)	Z_{ct} (km)	T_{cb} (°C)	T_{ct} (°C)	Z_e (km)	T_e (°C)	τ_c	Comments
** 25 April 1987	0229	N10	NSV	11.6	11.9	−62	−63	11.7	−62	0.004	
** 20 November 1987	2145	N9	SV	12.0	12.3	−52	−52	12.1	−52	0.009	
** 23 January 1988	2157	N9	TC	10.1	11.8	−51	−65	11.1	−59	0.106	Snowcover
** 21 February 1988	0303	N9	TV	10.1	11.9	−56	−66	11.4	−62	0.022	Contrails
** 23 May 1989	1525	N10	TC	9.7	11.5	−41	−53	10.8	−47	0.286	
** 7 June 1989	0015	N9	TV	9.8	10.6	−46	−48	10.0	−47	0.023	
** 24 October 1989	2135	N11	TC	10.1	11.8	−46	−57	11.1	−53	0.117	
14 November 1989	0306	N10	NSV	10.7	11.3	−56	−58	11.0	−56	0.010	
** 25 February 1990	2125	N11	TV	8.7	11.7	−41	−61	11.1	−58	0.067	Hazy
** 8 March 1990	0332	N10	NTC	9.2	12.2	−46	−51	10.1	−53	0.505	
16 March 1990	2125	N11	TV	10.9	11.3	−56	−56	11.0	−56	0.015	Contrails
4 April 1990	0324	N10	NTC	10.4	12.7	−55	−56	11.2	−60	0.196	Corona
** 6 April 1990	2102	N11	SV	10.7	11.4	−60	−59	11.0	−61	0.005	Corona
17 May 1990	0904	N11	NTC	8.4	11.7	−41	−61	10.1	−50	0.103	
3 June 1990	2051	N11	TV	11.3	13.5	−51	−60	12.0	−55	0.031	Corona
13 August 1990	1539	N10	TC	7.7	9.7	−22	−37	8.7	−30	0.079	
28 August 1990	0240	N10	TC	10.4	12.5	−40	−56	11.0	−43	0.128	
12 October 1990	2145	N11	TC	9.5	12.2	−39	−56	10.7	−47	0.158	22° Halo
** 9 November 1990	2130	N11	TV	11.8	14.1	−58	−70	13.0	−70	0.061	Corona
** 10 November 1990	0248	N10	NSV	13.1	14.0	−71	−71	13.5	−71	0.011	
** 7 February 1991	0155	N10	NSV	10.0	11.0	−54	−59	10.5	−58	0.033	Hazy, snowcover
28 February 1991	0211	N10	NSV	10.4	12.2	−56	−58	11.2	−60	0.063	
** 9 March 1991	2107	N11	TC	9.8	11.2	−52	−57	10.5	−56	0.052	
15 March 1991	0307	N10	NSV	8.3	9.3	−51	−57	8.9	−55	0.011	
17 March 1991	2118	N11	SV	6.9	7.5	−40	−44	7.2	−42	0.005	Corona
2 April 1991	2142	N11	SV	8.6	11.3	−40	−59	9.9	−51	0.035	
** 6 April 1991	0300	N10	TV	11.9	13.4	−60	−69	12.4	−63	0.095	
19 April 1991	0121	N10	SV	9.5	9.8	−50	−52	9.6	−51	0.002	
19 April 1991	1518	N10	SV	6.0	9.8	−27	−52	7.7	−39	0.072	
19 April 1991	2155	N11	SV	8.3	8.6	−44	−46	8.4	−44	0.003	

* SV = subvisual; NSV = nocturnal subvisual; TV = threshold visible; TC = thin cirrus; NTC = nocturnal thin cirrus
** = Project FIRE extended time observation

eter ξ, and the factors affecting $k/2\eta$. These variables not only impact on satellite cirrus retrieval approaches, but also have basic implications for lidar cirrus studies and climate research in general. Importantly, we offer an appraisal of τ_c in terms of the visual appearance of cirrus clouds.

Figure 3 shows the relationship between the optical (at the approximate 0.7-μm wavelength) and physical cloud thicknesses, where the five symbols correspond to our cirrus cloud categories (see figure insert). The expected increases in τ_c with increasing ΔZ and cloud visibility are clearly in evidence despite the considerable scatter present in the data points, which probably reflects both the complexity of cirrus development processes and the presence of random errors in our analysis approach. It should be noted that the indicated increase in τ_c with ΔZ is artificially limited to the values found appropriate for thin cirrus clouds.

As far as the delineation of τ_c with the various cirrus cloud categories is concerned, the results from Fig. 3 appear to confirm earlier lidar findings showing a $\tau_c \approx 0.03$ threshold for the visible detection of cirrus in the zenith (Sassen et al. 1989b; Sassen 1991a). Although threshold-visible cirrus data points are present to as low as $\tau_c \approx 0.01$, these cases are mainly associated with early afternoon observations in which high solar elevation angles increased the visibility of cirrus near the zenith (i.e., the cirrus tended to be invisible in other viewing directions, such that their total sky coverage would be underestimated by a surface observer). All thin cirrus occurrences fall within a 0.03–0.3 range of τ_c, indicating that cirrus with $\tau_c \gtrsim 0.3$ no longer appear bluish colored. The nocturnal measurements show results that are similar to the daytime threshold-visible versus thin cirrus data, which is not surprising in view of the reduced abilities to judge sky cloud cover at night using only stars as a guide. It can also be noted that subvisual and threshold-visible cirrus often display considerable geometrical thicknesses (up to nearly 4 km in this sample). Additional scatterplots (not shown) indicate no clear relationships between τ_c and ξ, Δ, or T_e.

The relative frequency of the parameter ξ is shown in Fig. 4 in the form of a histogram with $\xi = 0.1$ intervals. This cirrus sample clearly displays optical mid-cloud heights near the geometrical ($\xi = 0.5$) cloud center, although as the modal value of $\xi = 0.43$ indicates, the bottom half of the cloud (which contains 70% of

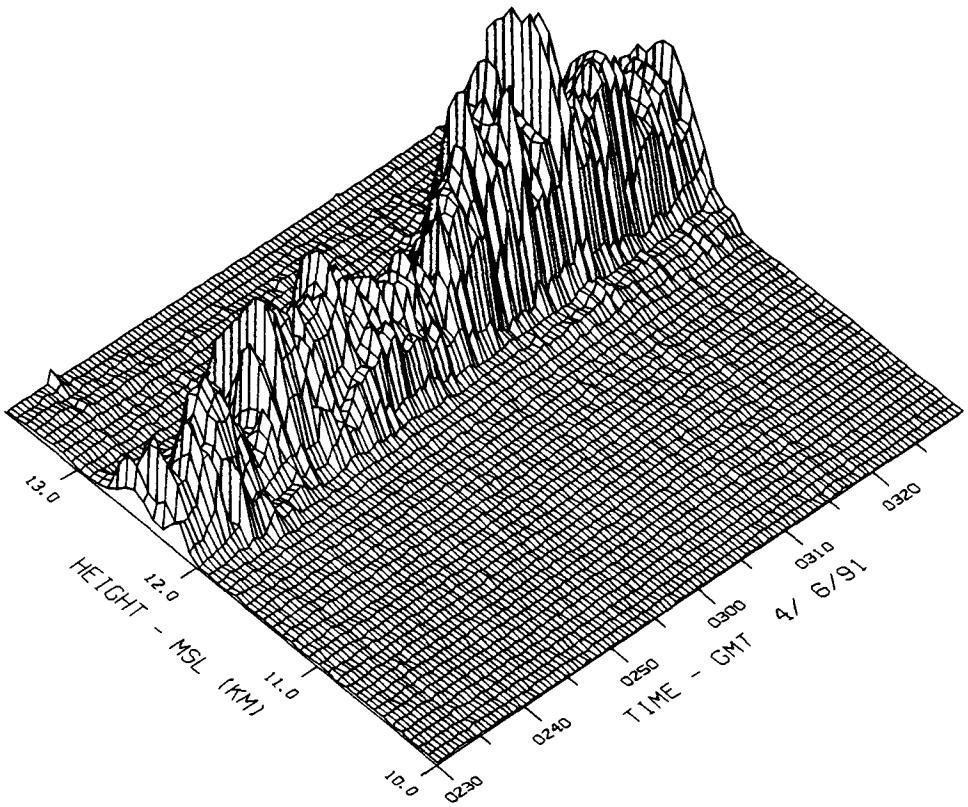

FIG. 1. Three-dimensional display of range-normalized laser signals (increasing upward in relative units) versus altitude and time for the threshold-visible cirrostratus sampled at the indicated date and times. The local overpass time of the N10 satellite was at 0300 UTC.

the points) tends to be more important radiatively. This finding would appear to reflect the strength of the ice precipitation process during cirrus cloud development (see Starr and Cox 1985), under the assumption that the accumulation of ice mass due to precipitation above the cloud-base region (where evaporation occurs) correspondingly dominates radiative effects. Also of likely importance, particularly for relatively deep cirrus layers, is the action of basic adiabatic cloud processes that increase ice-mass production with increasing temperature (see Heymsfield and Sabin 1989; Sassen and Dodd 1989). Our findings appear to be comparable with the mean backscatter profiles for cirrus clouds with geometric midcloud temperatures of less than −30°C (constituting nearly our entire sample), but differ significantly from those of the warmer cirrus reported by Platt et al. (1987). Perhaps the tendency for the warmer cirrus to display near-cloud-top scattering peaks in Platt et al. (1987) is due to relatively more active cloud-top particle-generating mechanisms, including the effects of supercooled liquid water layers at these temperatures.

The two derived lidar scattering parameters Δ and $k/2\eta$ are of considerable interest in terms of both assessing cirrus cloud content and improving the treatment of the lidar signal (see Platt et al. 1987). Both parameters contain information on the shapes, sizes, and orientations of cirrus particles. A long history of laboratory and field measurements has shown that backscatter linear depolarization data are inherently sensitive to the exact shape and orientation of hydrometeors (for a recent review see Sassen 1991b), and simple crystal habit (i.e., axial ratio) discrimination is also supported by theoretical ray-tracing simulations using several hexagonal crystal models (Takano and Jayaweera 1985; Takano 1987). Similarly, the variable $k/2\eta$ is influenced by crystal type through shape-related variations in the backscatter-to-extinction ratio (Takano 1987, personal communication), although in this case k is modified by such factors as lidar design and crystal size and concentration, which affect multiple scattering. Since, however, our understanding of the effects of realistic cloud microphysics on Δ and $k/2\eta$ is far from comprehensive, empirical findings are thus currently of importance, and we present in Figs. 5–9 a thorough evaluation of the lidar scattering properties (derived from method B) of the cirrus studied.

Shown in Fig. 5 is the dependence of integrated depolarization ratios on effective midcloud temperature, using the same five symbols for the cirrus cloud cate-

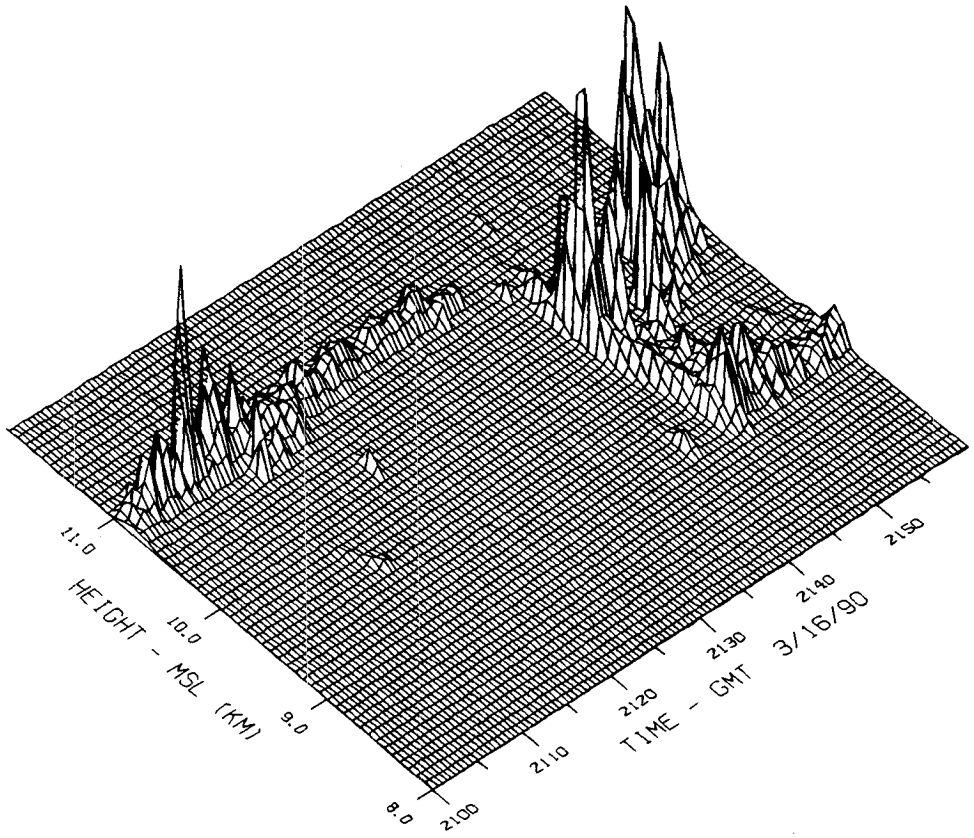

FIG. 2. As in Fig. 1 except that this cirrus is more variable in time and space. The N11 overpass occurred at 2125 UTC when a thin threshold-visible cirrus layer was present. Denser cirrus-generating cells and fallstreaks subsequently moved overhead.

gories in this and following figures as in Fig. 3. Also indicated are linear depolarization ratios representative of three simple ice-crystal habits derived from theory (Takano 1987), and the average midlatitude cirrus Δ (in 5°C intervals) measured by lidar in southeastern Australia by Platt et al. 1987. Most data points can be seen to fall within the range predicted for simple, randomly oriented crystals, and considering that horizontally oriented plate-crystal effects may be responsible for the atypically low Δ, the overall agreement with theory appears to be good. Although there is a tendency for Δ to decrease with decreasing temperature similar to the trend in the measurements of Platt et al. 1987, our values are noticeably higher at the lower temperatures.

To further explore the correspondence between theoretical predictions and our dataset, given in Fig. 6 is a scatterplot of $k/2\eta$ versus Δ. The locations of the symbols for thin plates (P, with a 10:1 diameter-to-thickness ratio), thick plates (T–P, 1.25:1), and long columns (C, 1:5) are based on theory including ice birefringence effects (Takano 1987), assuming that $\eta = 0.75$ describes the average case for our lidar application (see the Appendix). With this assumption it is clear that the majority of our data points can be ac-

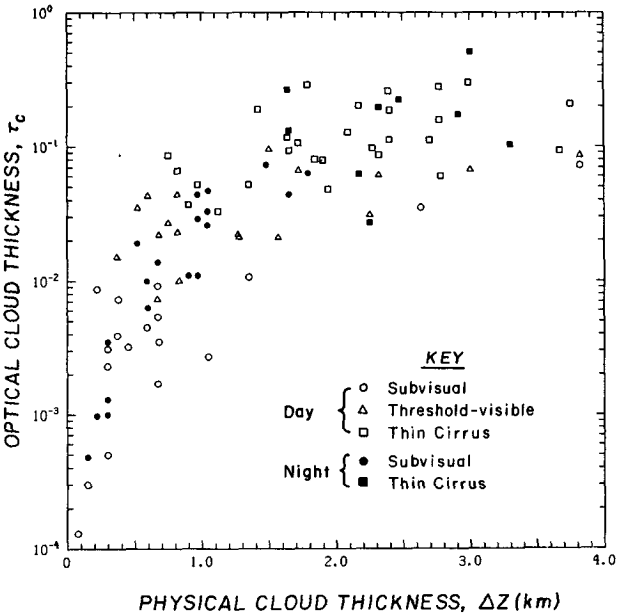

FIG. 3. Scatterplot of derived cloud optical thickness (at ~0.7-μm wavelength) versus physical cloud thickness, stratified in this and following figures (see insert) by the cirrus cloud categories defined in the text.

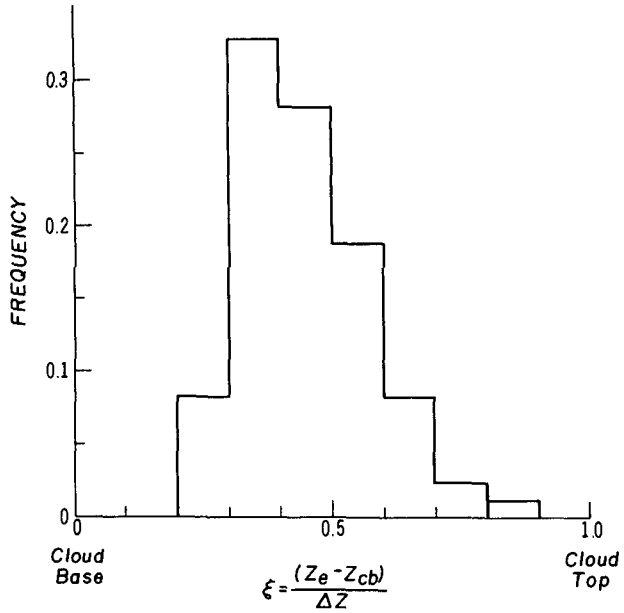

FIG. 4. Histogram of the frequency of occurrence of the variable ξ, showing that most optical midcloud heights occur within the lower half of subvisual–thin cirrus clouds.

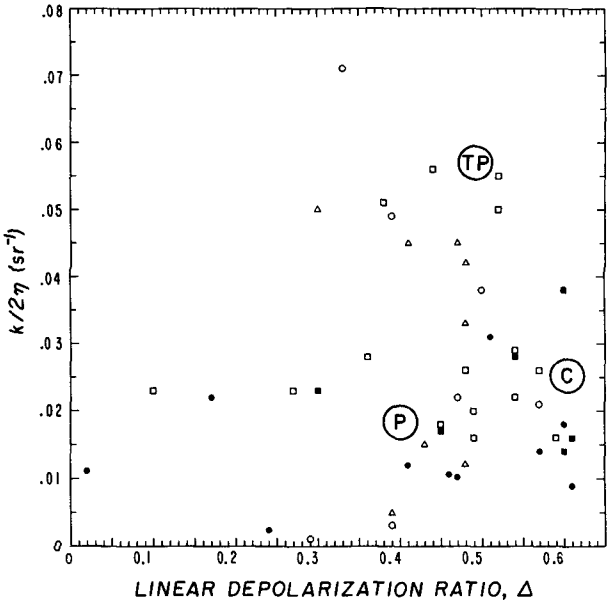

FIG. 6. Scatterplot of $k/2\eta$ versus Δ ratios for the five cirrus cloud categories (see Fig. 3), compared to the theoretically predicted domains for three typical ice-crystal habits, assuming $\eta = 0.75$ (appropriate for 200-μm mean cirrus particle equivalent diameters at our typical 3-mrad lidar receiver beamwidth).

counted for by various mixtures of simple ice-crystal types, which indeed appear to be appropriate for cirrus at these relatively low temperatures (Heymsfield and Platt 1984; Sassen et al. 1989a).

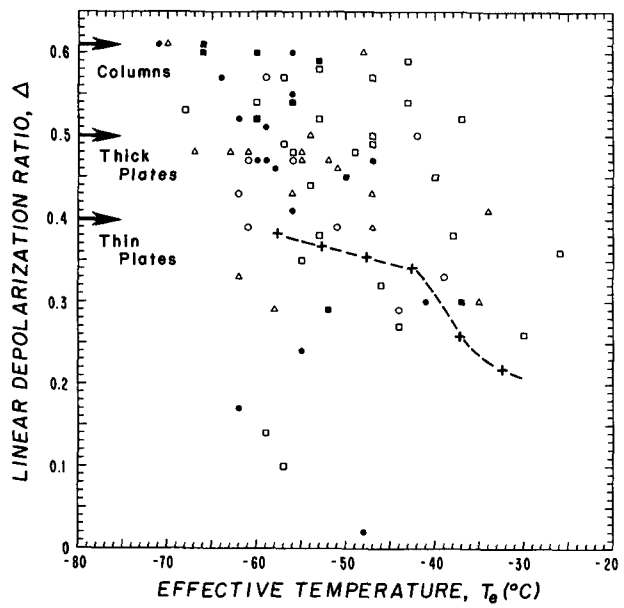

FIG. 5. The dependence of the vertically integrated linear depolarization ratio on the effective midcloud temperature, compared to the midlatitude cirrus findings of Platt et al. (1987) shown by the dashed line and "+" symbols. Arrows at left identify linear depolarization ratios derived theoretically for the indicated ice-crystal habits (from Takano 1987).

With the importance of the parameter $k/2\eta$ to lidar remote-sensing analysis (i.e., knowledge of this term eliminates two of the three unknowns in the standard lidar equation), we provide in Figs. 7 and 8 scatterplots of $k/2\eta$ versus effective cirrus cloud height and temperature, along with comparisons to the average findings of Platt et al. (1987) (dashed lines). Although our dataset of derived $k/2\eta$ is relatively small and displays scatter, the tendency for $k/2\eta$ to decrease with increasing altitude and decreasing temperature is clear and in apparent agreement with previous results. Note that Platt et al. (1987) reported different trends for summer and winter cirrus (the two dashed lines in Fig. 7), but because of our relatively low cirrus temperatures, it is appropriate only to point out that $k/2\eta$ seems to approach approximately 0.02 sr^{-1} at the colder temperatures and greater altitudes in both the Southern and Northern Hemisphere midlatitude cirrus samples.

Finally, a particularly illustrative display of cirrus cloud lidar scattering properties is given in Fig. 9, comparing τ_c with $k/2\eta$. Two interesting relationships are suggested but by no means conclusively demonstrated by the limited data. First, the nocturnal (i.e., filled-in) data points indicate that $k/2\eta$ values tend to be smaller at night than during daylight observations. This finding is also apparent in Figs. 7 and 8, which at the same time suggests that the nocturnal data points tend to be somewhat colder and higher. From Figs. 5 and 6, we also see that Δ tends to be higher for the lower temperatures and $k/2\eta$ values sampled in this study. Al-

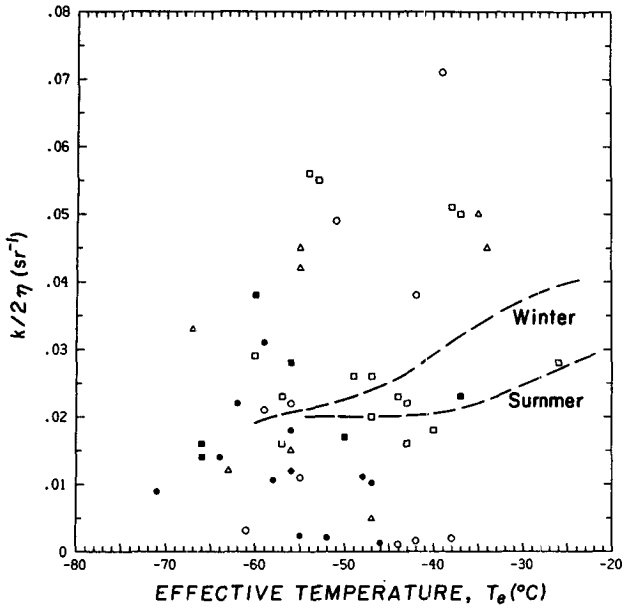

FIG. 7. Comparison of $k/2\eta$ ratios versus effective cloud temperatures with average results for winter and summer midlatitude cirrus clouds (dashed lines, as functions of cloud center temperatures) from Platt et al. (1987).

though these interdependencies could help account for the day–night differences in $k/2\eta$ of Fig. 9, $k/2\eta$ and Δ are both parameters that should respond to cirrus cloud microphysical variations induced by diurnal effects by virtue of their sensitivities to particle shape and size.

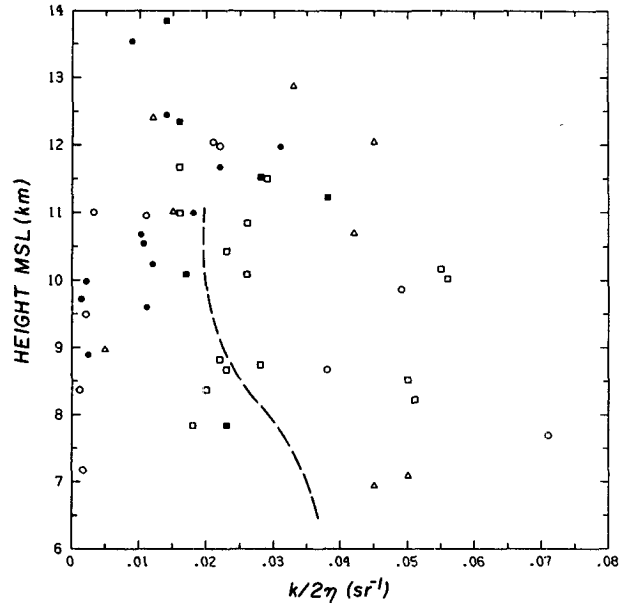

FIG. 8. Similar to Fig. 7, comparing our data points with the findings of Platt et al. (1987) (dashed line), but with respect to the dependence of $k/2\eta$ on cirrus midcloud height.

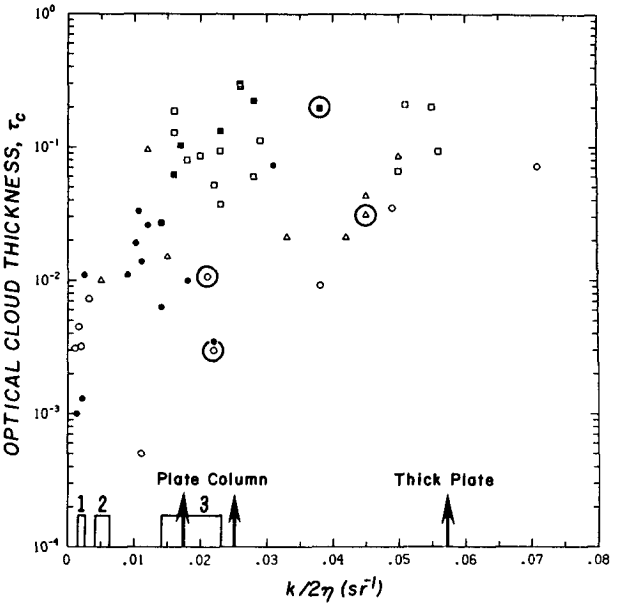

FIG. 9. The dependence of cirrus cloud optical thickness on $k/2\eta$, compared to theoretical predictions (arrows) from Takano (1987) for the indicated crystal habits, and the experimental results for minute simple ice crystals ("1," Sassen 1978; "2," Sassen and Liou 1979), and spatial ice particles ("3," Sassen 1978). Symbols enclosed by circles represent corona-producing cirrus clouds.

The fact that values of $k/2\eta$ for many subvisual cirrus clouds are quite small ($\leq$0.005 sr^{-1}) is also interesting, but apparently not inconsistent with previous empirical results. This class of weakly scattering cirrus generally yielded $\Delta \approx 0.3$–0.4 and tended to occur at temperatures between approximately $-40°$ and -55°C. (In other words, they are dissimilar from the subset of cirrus that produce corona displays, which according to Fig. 9 yielded much higher $k/2\eta$.) It is possible that they are composed of particles even smaller than those associated with the corona-producing cirrus (i.e., ~20-μm mean diameter), such that geometric optics scattering assumptions are violated and unexpectedly low k are generated. This view is supported by laboratory evidence for reduced k values for relatively minute ice-crystal populations (Sassen 1978; Sassen and Liou 1979), as shown in Fig. 9.

5. Conclusions

Although we acknowledge that the subvisual–thin cirrus cloud dataset described here is limited in extent, compared to the extensive observations we are compiling in support of the ongoing Project FIRE, it is not premature to present preliminary findings that address an important and timely topic—the basic characteristics of cirrus clouds that can often escape detection by ground observers or from satellites. Current climate models require improved cloud characterization inputs

based on traditional surface data, and, awaiting long-term advanced surface or earth-orbiting remote-sensing cloud climatologies, the means to improve basic cirrus cloud parameterizations (e.g., in terms of τ_c) are crucial to modeling efforts directed toward predicting climate change.

The chief purposes of this report are twofold. The first is to provide researchers with a critically described set of remote-sensing data coincident with local NOAA polar-orbiting satellite overpasses to help test cirrus cloud retrieval algorithms and establish the limits of cirrus detectability from available satellite radiance measurement methods. Pertinent data for 30 overpasses, which span the (day and night) subvisual–thin cirrus cloud categories under various atmospheric conditions, are provided in Table 1. Second, it is hoped that our characterizations of the mean properties of this neglected group of cirrus clouds will advance our ability to treat their effects in lidar and basic climate research.

Based on our findings, we offer the following characterizations for cirrus clouds in terms of τ_c: for subvisual cirrus $\tau_c \leqslant 0.03$, for threshold-visible cirrus (a category depending mostly on lighting conditions and spatial cloud uniformity) $0.01 \leqslant \tau_c \leqslant 0.1$, and for thin (bluish-colored) cirrus $0.03 \leqslant \tau_c \leqslant 0.3$. During nocturnal observations, $\tau_c \approx 0.05$ can be considered to separate cirrus causing noticeable reductions in the numbers of visible stars from lesser interference, which could be, for example, attributable to lower-atmospheric turbidity and light pollution effects. We may also extend our results to optically thicker cirrus clouds on the basis of knowledge gained during the 1986 Project FIRE intensive field observations (Kinne et al. 1992). It was found that lidar-derived τ_c tended to saturate at approximately 2.0–3.0 in dense cirrostratus, which visually appeared dark, lacked halos, and also caused the solar disk to appear dim and irregular. Clearly, these characteristics define an altostratus cloud, so we can finally group all remaining (i.e., opaque) cirrus into a $0.3 \leqslant \tau_c \leqslant 3.0$ category. An empirically based definition for altostratus of $\tau_c \gtrsim 3$ then follows.

The previously determined visible versus subvisual threshold of $\tau_c \approx 0.03$ (Sassen et al. 1989b; Sassen 1991a) and the 0.06 value for a threshold-visible cirrus (Platt et al. 1987) are thus supported by this larger data sample. Our current approaches involve the application of an apparently new analysis method using $k/2\eta$ as a variable and also employ the full range of theoretically predicted k values, but it should be acknowledged that the same basic assumptions and equations have been relied on in all our studies. It is also apparent that the selection of this threshold τ_c from Fig. 3 represents only an approximation in view of the scatter in the data points and the various factors affecting cirrus cloud visibility. Nonetheless, we believe that we have adopted the soundest approach possible using our conventional lidar measurement capabilities and are encouraged by the general similarity between our $k/2\eta$ for typical cirrus and the mean values derived from a larger cirrus sample (and using a different approach) by Platt et al. (1987), as functions of altitude and temperature (see Figs. 7 and 8). On the other hand, we have identified the presence of a class of radiatively distinct subvisual cirrus that display atypically low ($\leqslant 0.005$ sr^{-1}) $k/2\eta$ ratios and do not feel as confident in the τ_c derived on the basis of theoretical ray-tracing k values. The low values of $k/2\eta$, however, are in compliance with the scattering behavior of laboratory-grown populations of minute simple ice crystals.

The significance of the apparent day-versus-night differences in $k/2\eta$ (Fig. 9) may be questionable in view of the small sample size, but we believe that this parameter is a particularly good candidate to reflect the kinds of diurnal cloud microphysical alterations that numerical simulations treating cloud–radiative feedbacks have predicted (Starr 1987). Cloud model results have revealed significant day–night differences in the ice water budget and convective structure of thin cirrus clouds that are regulated by radiative processes. A considerably more rigorous examination of the ensuing effects on lidar scattering than can be evaluated here is needed, but it is likely that the corresponding changes in the concentrations, shapes, and sizes of ice crystals (with or without convective–cloud feedbacks) will be manifested by changes in $k/2\eta$. Similarly, linear depolarization is quite sensitive to ice crystal shape, and it is possible that the tendency for higher Δ values to occur at night (Fig. 5) is also in some way a result of radiative effects on ice-crystal nucleation and growth. Future studies based on our entire and enlarging cirrus cloud ETO sample will allow for a more comprehensive statistical analysis of such factors.

Finally, it seems appropriate at this point in the development of various ground-based cirrus cloud climatologies (see also the recent results of Imasu and Iwasaka 1991) to consider the broader issue of the representativeness, in terms of global climate concerns, of these relatively few datasets. Certainly, the synoptic conditions responsible for the generation of cirrus differ widely according to season, latitude, and landmass influences. Platt et al. (1987) have described significant differences not only in midlatitude and tropical cirrus properties, but also between winter and summer midlatitude cirrus. Although our subvisual–thin cirrus cloud sample is probably biased somewhat toward higher and colder cirrus than is typical of our region (i.e., they could often represent the tops of deeper cirrus systems), the temperatures, heights, and depolarizing properties of the two midlatitude cirrus samples appear sufficiently dissimilar to suggest the presence of basic differences in the high cloud components sampled. It is important to recognize that the results of extended-time surface-based observations of cloud properties will likely tend to be site specific before applying the findings to regional or zonal scales.

Acknowledgments. Recent support for our FIRE and ECLIPS research has been provided by NSF Grant ATM-8914348 and NASA Grant NAG-1-868, and for thin cirrus studies supporting DMSP by award numbers 50112 and 50113 from The Analytic Sciences Corporation.

APPENDIX

Data Analysis Uncertainties

The findings reported here are subject to well-known uncertainties associated with the basic assumptions required to solve the lidar equation using conventional lidar data. Fortunately, the resultant errors in derived data quantities tend to be minimized when optically thin ice clouds are treated, primarily because the effects of laser pulse attenuation and multiple scattering are considerably less important than those in the denser clouds of the lower atmosphere. (Thus, the thin cirrus situation approaches the relative simplicity of microwave radar studies of weakly attenuating targets.)

Both methods A and B for solving the lidar equation in terms of $\beta'_c(z)$ are founded on the "clean-air" scattering assumption, in which the boundary condition is provided by Rayleigh-scattering predictions for the pure molecular atmosphere (as in Fernald et al. 1972) at some height z_0 below cloud base corresponding to the range-normalized lidar signal minima $S(z_0)z_0^2$.

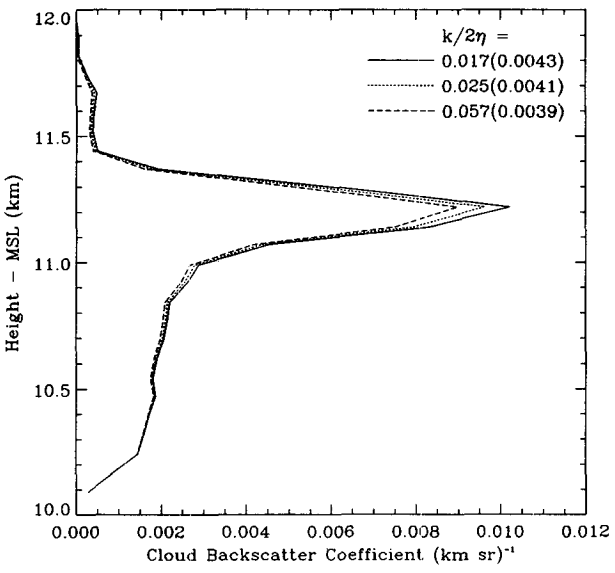

FIG. A1. Effects on derived backscatter coefficient profiles [and vertically integrated β'_c (sr^{-1}) in parentheses] induced by varying $k/2\eta$ (sr^{-1}) over the indicated range for a thin cirrus cloud studied on 23 January 1988 (see Table 1). This cirrus displays an unusually strongly scattering cloud-top layer, but only minor differences in the results are evident over this range of $k/2\eta$.

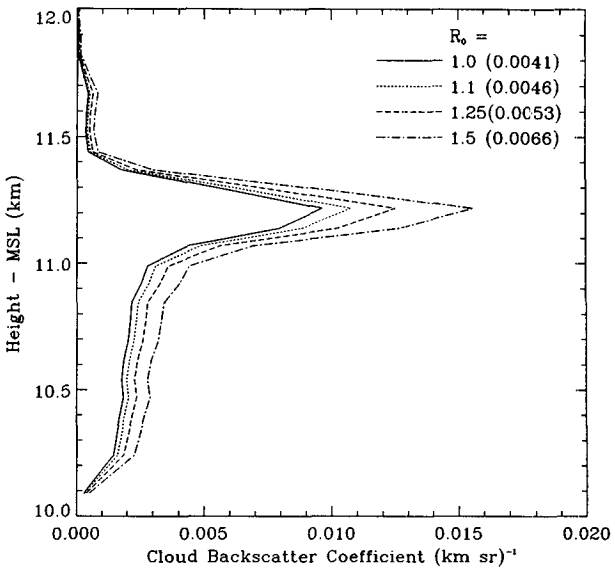

FIG. A2. Effects on $\beta'_c(z)$ profiles and integrated β'_c (as in Fig. A1, but using only the intermediate $k/2\eta = 0.025\ sr^{-1}$) produced by violating the "clear-air" scattering assumption. In these simulations the aerosol-enhanced subcloud boundary is expressed in terms of the indicated initial scattering ratios R_0.

The governing equation (from Sassen et al. 1989b) is given by

$$\beta'_c(z) = \frac{G(z_0, z)}{1 - 2\dfrac{\eta}{k}\displaystyle\int_{z_0}^{z} G(z_0, z')dz'} - \beta'_m(z), \quad \text{(A1)}$$

where

$$G(z_0, z) = \beta'_m(z_0)\frac{S(z)z^2}{S(z_0)z_0^2} \times \exp\left[2\left(\frac{8\pi}{3} - \frac{\eta}{k}\right)\int_{z_0}^{z}\beta'_m(\xi)d\xi\right].$$

There are several sources of uncertainty with this inversion method, but Fig. A1 illustrates that the basic uncertainties in the β'_c profiles derived from a typical thin cirrus cloud (average $\tau_c = 0.11$) are not significant. Since the optical attenuation suffered by the laser pulse in traversing the diffuse scattering medium has a relatively small effect on the inversion, uncertainties in specifying η and k within likely ranges (see the following) do not contribute to large variations in $\beta'_c(z)$. The β'_c profiles in Fig. A1 were generated from method A computations with $k/2\eta$ varying over the standard range of 0.017–0.057 sr^{-1}. The resultant changes in the integrated backscatter coefficients are shown in parentheses.

The validity of the clear-air-scattering boundary condition itself, however, should be questioned and the possible errors examined. Strictly speaking, scat-

tering ratios of $R = 1.0$ should not be presumed to exist anywhere in the troposphere, so that the question becomes to what extent this basic assumption can be violated without generating significant errors from Eq. (A1). Figure A2 provides such an assessment (as in Fig. A1, except that a single $k/2\eta = 0.025$ sr^{-1} is treated) as R at z_0 is increased from 1.0 to 1.5. Errors produced by uncertainties in the boundary condition are tolerable at this wavelength as long as the aerosol scattering component remains, say, less than one-quarter of the molecular scatter (i.e., $R_0 \leq 1.25$) at the minimum lidar signal, which is probably a valid assumption in the upper half of the troposphere (in the absence of episodic volcanic aerosol fallout). However, the regular use of $R_0 = 1.0$ would tend to systematically overestimate τ_c somewhat. The related source of uncertainty attributable to the treatment of signals to derive a representative $S(z_0)z_0^2$ has been minimized through the results of simulations aimed at optimizing the spatial and temporal averaging schemes in real signals, so that only minor random errors are expected from our high-power lidar returns.

On the other hand, Eq. (3) illustrates that the accuracy of the derived τ_c is linearly dependent on the choice of the value of k used (in addition to the minor effects on integrated backscatter). We believe, however, that our approach to represent τ_c as the average of bracketing solutions using currently available k (based on theoretical and experimental findings) will on average provide meaningful results in our cirrus cloud sample.

Finally, implicit in these formulations is the assumption that multiple-scattering effects on the lidar equation inversion are adequately compensated for by reducing the impact of laser pulse attenuation through the specification of a $\eta = 0.75$. According to recent lidar-return simulations (Sassen et al. 1992), this is only a partial solution to the multiple-scattering problem, since in addition to the "captive-diffraction" effects specified by η, an extra backscatter coefficient dominated by double scattering into the near-backward direction should also be considered. At present, in consideration of the dominant forward scattering in the cirrus particle phase function, and awaiting cirrus cloud scattering simulations tailored to our lidar system, we have assumed that the latter scattering component is relatively unimportant in the diffuse subvisual and thin cirrus cloud environment. Note that the arbitrary $\eta = 0.75$ value used here is based on the proportion of diffracted energy, from an ice particle with an assumed 100-μm radius, that would remain indefinitely within the 3-mrad lidar receiver field of view normally used in our FIRE ETO cirrus studies. This equivalent particle size represents our best judgment in cirrus that lack the more active precipitation development in denser, and generally warmer, cirrus cloud systems (see Heymsfield and Platt 1984; Sassen et al. 1989a).

REFERENCES

Fernald, F. G., B. M. Herman, and J. A. Reagan, 1972: Determination of aerosol height distributions by lidar. *J. Appl. Meteor.*, **11,** 482–489.

Grund, C. J., and E. W. Eloranta, 1990: The 27–28 October 1986 FIRE IFO cirrus case study: Cloud optical properties determined by high spectral resolution lidar. *Mon. Wea. Rev.*, **118,** 2344–2355.

Heymsfield, A. J., and C. M. R. Platt, 1984: A parameterization of the particle size spectrum of ice clouds in terms of the ambient temperature and the ice water content. *J. Atmos. Sci.*, **41,** 846–855.

——, and R. M. Sabin, 1989: Cirrus crystal nucleation by homogeneous freezing of solution droplets. *J. Atmos. Sci.*, **46,** 2252–2264.

Imasu, R., and Y. Iwasaka, 1991: Characteristics of cirrus clouds observed by laser radar (lidar) during the spring of 1987 and the winter of 1987/88. *J. Meteor. Soc. Japan,* **69,** 401–411.

Kinne, S., T. P. Ackerman, A. J. Heymsfield, F. D. J. Valero, K. Sassen, and J. D. Spinhirne, 1992: Cirrus microphysics and radiative transfer. Cloud field study on 28 October 1986. *Mon. Wea. Rev.*, **120,** 661–684.

Liou, K. N., 1986: Influence of cirrus clouds on weather and climate processes: A global perspective. *Mon. Wea. Rev.*, **114,** 1167–1199.

Platt, C. M. R., 1979: Remote sounding of high clouds. Part I: Calculation of visible and infrared optical properties from lidar and radiometer measurements. *J. Appl. Meteor.*, **18,** 1130–1143.

——, J. C. Scott, and A. C. Dilley, 1987: Remote sounding of high clouds. Part VI: Optical properties of midlatitude and tropical cirrus. *J. Atmos. Sci.*, **44,** 729–747.

Sassen, K., 1978: Backscattering cross sections for hydrometers; measurements at 6328Å. *Appl. Opt.*, **17,** 804–806.

——, 1991a: Corona-producing cirrus cloud properties derived from polarization lidar and photographic analyses. *Appl. Opt.*, **30,** 3421–3428.

——, 1991b: The polarization lidar technique for cloud research: A review and current assessment. *Bull. Amer. Meteor. Soc.*, **72,** 1848–1866.

——, and G. C. Dodd, 1989: Haze particle nucleation simulations in cirrus clouds, and applications for numerical and lidar studies. *J. Atmos. Sci.*, **46,** 3005–3014.

——, and K. N. Liou, 1979: Scattering of polarized light by water droplet, mixed phase and ice crystal clouds: II. Angular depolarizing and multiple scattering behavior. *J. Atmos. Sci.*, **36,** 852–861.

——, D. O'C. Starr, and T. Uttal, 1989a: Mesoscale and microscale structure of cirrus clouds: Three case studies. *J. Atmos. Sci.*, **46,** 371–396.

——, M. Griffin, and G. C. Dodd, 1989b: Optical scattering and microphysical properties of subvisual cirrus clouds, and climatic implications. *J. Appl. Meteor.*, **28,** 91–98.

——, H. Zhao, and G. C. Dodd, 1992: Simulated polarization diversity lidar returns from water and precipitating mixed phase clouds. *Appl. Opt.*, **31,** 2914–2923.

Schiffer, R. A., and W. B. Rossow, 1983: The International Satellite Cloud Climatology Project (ISCCP): The first project of the world climate research programme. *Bull. Amer. Meteor. Soc.*, **64,** 2682–2694.

Starr, D. O'C., 1987: Effects of radiative processes in thin cirrus. *J. Geophys. Res.*, **92,** 3973–3978.

——, and S. K. Cox, 1985: Cirrus clouds. Part II: Numerical experiments on the formation and maintenance of cirrus. *J. Atmos. Sci.*, **42,** 2682–2694.

Takano, Y., 1987: Multiple scattering of polarized light in cirrus clouds. Ph.D. dissertation, University of Utah, 126 pp.

——, and K. Jayaweera, 1985: Scattering phase matrix for hexagonal ice crystals computed from ray optics. *Appl. Opt.*, **24,** 3254–3263.